EXERGY BASED DESIGN METHODOLOGY FOR AIRFOIL SHAPE OPTIMIZATION AND WING ANALYSIS

Haipeng Li*, Jason Stewart, Richard S. Figliola***
***Clemson University, **General Electric**

Keywords: *Exergy Entropy Optimization Airfoil Wing*

Abstract

This paper applies an exergy-based method on the two-dimensional airfoil and various three-dimensional wing planforms to investigate the impact of exergy on aerodynamic designs. Our intent here is to report our efforts to couple a numerical code with an exergy analysis, a shape shifting algorithm and an optimization code to achieve desired airfoil and wing shapes. Exergy-based optimization is performed to minimize entropy generated on simple airfoils under turbulent flow conditions. Entropy generation and its relationship to total and induced drag are studied for different twisted wing shapes.

Nomenclature

ρ	density
Φ	viscous dissipation
μ	dynamic viscosity
τ	shear stress
δ	Kronecker delta
∞	subscript for reference state
Cd	drag coefficient
Cl	lift coefficient
E_d	Exergy destruction
F_d	Drag force
P	static pressure
Re	Reynolds number
S'''_{gen}	volumetric entropy generation rate
S_{gen}	total entropy generation rate
T	temperature
h	specific enthalpy
i	tensor index
j	tensor index
h	specific enthalpy
t	time
u	streamwise velocity component
v	vertical velocity component
w	spanwise velocity component
x	streamwise direction
y	vertical direction
z	spanwise direction

1 Introduction

There is a growing interest in the potential use of exergy-based strategies for aircraft systems integration and design. The approach focuses on the useful component of energy, i.e. exergy, necessary to operate the system. Since energy is somehow required for the functioning of any system, exergy naturally becomes a common tool for system designs. According to the second law of thermodynamics, exergy is not conserved during any real process. It is consumed to meet system objectives and some is irreversibly destroyed. The destruction of exergy is proportional to the corresponding entropy generation. Minimizing entropy generation leads to better use of exergy. That is why entropy generation minimization (EGM) methods have been used for many thermodynamic optimization problems.

At the heart of exergy-based systems integration is the analytical methods used to characterize each system and to optimize within and between systems. As a start, we look at optimizing two-dimensional (2-D) airfoil shapes in such a way that we can determine the best shape for aircraft mission segments. We also examine the three-

dimensional wing in terms of entropy generation and its relationship to total and induced drag. In concomitant studies, we are looking at the broader problem of integrating the three-dimensional aerodynamic shape optimization with shape controller models and intersystem energy flows to develop optimal shape shifting strategies. The overall purpose of the study is to present a tool for significant analysis and optimization into a design format.

Two dimensional airfoil shape design is a classical problem in the aerospace industry. However, there have been few efforts to use the entropy minimization method for airfoil shape optimization. In this paper, we report on efforts to use a computational fluid dynamics (CFD) solver, which includes an assessment of full field entropy generation, to optimize 2-D airfoil shapes with imposed constraints, such as maximum lift/drag ratio. We perform a two-objective optimization on the 2-D airfoil using a genetic algorithm based optimization scheme. Our intent here is to report our efforts to couple the numerical code with a shape shifting algorithm and optimization code. Another aspect of our study is the entropy generation evaluation in three-dimensional domain. We developed a unique approach of control volume analysis to relate exergy destruction to drag in low subsonic flows. Future work to optimize wing shapes based on exergy-based analysis is underway. In a previous study [7], we examined a similar approach but with laminar flow only. In this paper, we will expand it to the fully turbulent flow and examine the issue of accuracy that arises with turbulent modeling.

2 Approach

2.1 Flow Solver

The numerical simulations use the general viscous equations represented in a Reynolds-averaged (RANS) form written as:

$$\frac{\partial \rho}{\partial t} + \frac{\partial \rho u_i}{\partial x_i} = 0 \qquad (1)$$

$$\frac{\partial \rho u_i}{\partial t} + \frac{\partial}{\partial x_j}(\rho u_i u_j) = -\frac{\partial P}{\partial x_i} + \frac{\partial \tau_{ij}}{\partial x_i} + \frac{\partial}{\partial x_j}(-\rho \overline{u_i' u_j'}) \qquad (2)$$

$$\tau_{ij} = \left[\mu \left(\frac{\partial u_i}{\partial x_j} + \frac{\partial u_j}{\partial x_i} \right) \right] - \frac{2}{3} \mu \frac{\partial u_l}{\partial x_l} \delta_{ij} \qquad (3)$$

The local entropy generation rate (W/K-m^3) in a three-dimensional flow field is arrived by a balance of the conservation equations and the second law of thermodynamics across a differential fluid volume and results in the positive accruing general form[1]:

$$\dot{S}'''_{gen} = \frac{k}{T^2}(\nabla T)^2 + \frac{\mu}{T}\Phi \qquad (4)$$

with the viscous dissipation term given by

$$\Phi = 2\left[\left(\frac{\partial u}{\partial x}\right)^2 + \left(\frac{\partial v}{\partial y}\right)^2 + \left(\frac{\partial w}{\partial z}\right)^2\right] + \left[\left(\frac{\partial u}{\partial y} + \frac{\partial v}{\partial x}\right)^2 + \left(\frac{\partial u}{\partial z} + \frac{\partial w}{\partial x}\right)^2 + \left(\frac{\partial v}{\partial z} + \frac{\partial w}{\partial y}\right)^2 \right] \qquad (5)$$

Therefore entropy generation is not calculated directly but is calculated from other properties. The second term in Equation 4 develops directly as a consequence of the velocity field around a moving body. The spatial information required to calculate this term is available from the full field viscous solver. It directly couples the flow field fluid dynamics with exergy. The first term results from thermal convective exchange between the body and its surroundings through direct or indirect means including internal and aerodynamic heating. It becomes important with high-speed aircraft or any aircraft using thermal methods, such as shape memory alloys, to implement shape change.

In laminar flows, the exact velocity field is directly obtained from the RANS solver so that Equation 4 can be used without modification. However, in turbulent flow, only the mean velocity profiles are given in the RANS solver. To account for the fluctuating velocity contribution, the effective viscosity, which is the sum of the laminar viscosity and the turbulence viscosity, replaces the laminar viscosity in Equation 4. It is in this manner that Drost and White [4] suggest extracting the local entropy rate from an existing numerical code; they applied it on an impinging jet. Shuja, et.al. [9] used the same minimum entropy concept on an impinging jet flow to evaluate various turbulence models. They report a dependency between the turbulence model used and the entropy generation estimate. This is a consequence of the differing estimates of the effective viscosity used in the different models. In the previous study [7], we greatly simplified things by assuming the laminar flow case so as to separate the turbulence model issue from the logistical steps to couple the numerical model with a shape shifting algorithm and the optimizer. In this paper, we address the approximation of the entropy generation using effective viscosity and compare the results versus experimental data.

2.2 Entropy generation in turbulent flow using CFD

First let's examine entropy generation calculation in turbulent pipe flow as shown in Figure 1. Instead of showing entropy generation, the turbulent dissipation, which is the essential part of entropy generation, is shown. Bejan [1] derives an expression for turbulent dissipation in turbulent pipe flow and it was compared with CFD results. Bejan's equation is for fully developed turbulence of infinite Reynolds number. We compare it with three cases of different Reynolds number. It can be seen for all three cases, the calculated turbulent dissipation has a good match in the region close to the wall, where high values are observed. There is some deviation away from the wall, which is due to the approximation nature of RANS solver. The exact turbulent dissipation is composed of the gradient of both mean velocity and fluctuating velocity. However, fluctuating velocity is not present in RANS solver, instead, it is replaced by turbulence models. The modeling is an approximation and causes deviation from exact results. Nonetheless, as can be seen in the following test case, this approximation performs very well in predicting the drag on an airfoil.

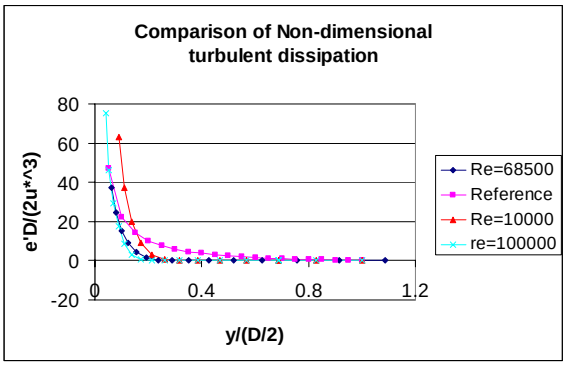

Fig 1. Turbulent Dissipation Comparison

Next we chose a NACA0012 as the benchmark airfoil as it is well documented in the open literature. By comparing lift, drag and entropy generation from a numerical calculation, we are able to verify and validate the modeling/computational procedure.

We modeled the NACA0012 in a wind tunnel with compressible flow. The freestream Mach number was set to be 0.2 and the ideal gas model was used for the fluid material. Running a case at three degrees of angle of attack, we obtained a lift coefficient of 0.3561, about 8% deviation from the thin airfoil theoretical value. The drag coefficient from surface integration is 113 drag counts (one drag count is 1/10000 of drag coefficient Cd), which is 64% higher than the experimental value. This is due to a well-known phenomenon of the over prediction of drag, present in all CFD solvers, and related to the surface integration method used. However, if we calculate the drag coefficient from entropy generation, it brings down the number

to 92 drag counts, almost half. Although it still over predicts the drag, it is much better than the traditional surface integration over the airfoil. In another case study, if we turned on the two layer approach, which essentially sets up a laminar zone around the leading edge, we see even better results in term of drag and entropy generation related drag. Therefore, we are confident to say that entropy generation in turbulent flow using the effective viscosity leads to a good approximation of the expected value.

2.3 Drag and entropy generation

Based on literatures and our study, we found that the drag and entropy generation in 2-D domain can be related by Equation 6. This is essential because drag can be directly estimated from entropy generation without other effects. The next section further shows this approach is also better and more accurate.

$$D = \frac{\iiint_{v} S'''_{gen} dv \times T_{\infty}}{U_{\infty}} \qquad (6)$$

2.3.1 Two-dimensional study

Two pipe flow cases are selected as examples within a two dimensional domain and the flow conditions and results are shown in Table 1. Both laminar flow and turbulent flow are studied. For each flow, two meshes are used. One coarse mesh is 100 by 20 and a finer mesh is 100 by 40. Air with constant densityand constant viscosity is used as the working fluid. Velocity is set to be constant. Flow fields are solved using a RANS solver – Fluent. Using the obtained velocity field, entropy generation and drag force from surface force integration on the airfoil are calculated. Here we use the surface integration technique to estimate drag as the benchmark because the flows are simple and the walls in the pipe are not curved so that CFD predicts drag on a pipe very well. Drag force from entropy generation using Equation 6 is compared with drag calculated using surface integration and is shown in the last two columns in Table 1. It can be seen they match very well with each other. These test cases verify that drag can be estimated from entropy generation with very high accuracies.

Grid Spacing	Sgen(W/K)	Drag from surface integration	Drag from Sgen	% drag diff
100*40	0.006795923	2.075	2.0387769	1.75%
100*40(tur)	0.00680896	2.073265	2.042688	1.47%
100*20	0.006793336	2.066852	2.0380008	1.40%
100*21(tur)	0.006806631	2.067505	2.0419893	1.23%

Table 1 Sgen vs Cd for Pipe Flows

2.3.2 Three-dimensional(3-D) study

The objective of linking exergy destruction to drag was extended to the 3-D domain as well. Here a method for calculating drag on a finite wing is introduced and applied to three different wing shapes.

Linking exergy destruction to drag in a CFD simulation is identical in the 2-D and 3-D case. However, due to the induced drag contribution in a 3-D model special attention must be given to calculating entropy generation. This is because the trailing wing tip vortex, for example, may extend very far downstream of the wing. In many CFD models it is computationally prohibitive to model the flowfield far enough downstream of the wing such that the velocity perturbations caused by the wing are damped out. As a result a simple volume integration within the computational domain to calculate entropy generation is not sufficient to determining drag of a wing.

The first step in the process of determining drag by calculating entropy generation as a result of the presence of the wing is to perform a volume integration of the viscous dissipation term within the CFD domain and together with Equation 4 an estimate for the entropy generation within the

model is obtained. The next step is to obtain an estimate for the projected entropy generation seen in the flow after it leaves the CFD domain. This is accomplished by performing an exergy balance over a volume situated directly downstream of the CFD domain. Calling the downstream control volume CV2 the resulting exergy balance over CV2 is:

$$\dot{E}_d = \int_2 \rho u_2 (h_2 - T_\infty s_2 + \frac{u_2^2 + v_2^2 + w_2^2}{2})\, dA - \int_3 \rho u_3 (h_3 - T_\infty s_3 + \frac{u_3^2}{2})\, dA \qquad (7)$$

Here surface 2 is the entrance of CV2 (or equivalently the exit of the CFD domain), and surface 3 is the exit of CV2.

By assuming the following:

1.) The sides of the CFD domain are far enough away from the wing that negligible flow leaves through any surface other than the inlet and outlet

2.) Surface 3 is far enough downstream that the velocity profile is approaching that of the freestream velocity, i.e. $u_3 \rightarrow U_\infty$ as $x \rightarrow \infty$

3.) All flow properties are constant on surface 3

4.) Temperature and density stay nearly constant (all flow studies performed at Mach 0.2 here)

The steady state exergy destruction rate for CV2 is:

$$\dot{E}_d = \int_2 \rho u_2 \frac{v_2^2 + w_2^2 + (U_\infty^2 - u_2^2)}{2}\, dA \qquad (8)$$

Combining this with the entropy volume integration, and utilizing Equation 6 we obtain the following relation for drag force in low speed flows.

$$F_D = \frac{1}{U_\infty}(T_\infty \int_{CV} \dot{S}'''_{gen}\, dV + \int_{outlet} \rho u_2 \frac{v^2 + w^2 + (U_\infty^2 - u^2)}{2}\, dA) \qquad (9)$$

Here, outlet corresponds to the exit surface of the volume used for the volume integration represented by CV in the first integral.

2.3 Turbulent models

As we discussed earlier, because of turbulent modeling, the evaluation of entropy generation in CFD is not exact. Instead, it is just an approximation of the precise one. This naturally leads to a question: which turbulent model gives us the best results in terms of the entropy generation calculation? A series of cases are done to investigate this aspect. We found that Fluent's low Reynolds (Low-Re) number K-ε modes are among the best. Fluent provides 6 Low-Re K- ε models. In the results shown in Table 2, they are all tested using the same mesh and boundary conditions. Similar to previous sections, drag and entropy generation (S_{gen}) are compared with their corresponding experimental values, either directly (drag) or indirectly (S_{gen}, using drag and S_{gen} relation equation). It can be seen that except model 3, all other models perform very well. Model 5 is the best performer but it's not too much deviated from others.

3 Results

3.1 2-D Airfoil optimization

An optimization of airfoil shape based on entropy generation minimization was accomplished. The airfoil shapes are represented by NURBS curve. The basis airfoil is based on Li's [8] study but only 18 control points were selected to simplify the process. 6 out of 18 points were allowed to move within a

specified range to change the airfoil shape. We chose three control points on the top surface of the airfoil and three control points on the bottom surface of the airfoil. To help keep the optimization solution within bounds, we apply a constraint of a fixed chord. Both leading edge and trailing edge points are fixed, so the chord remains constant. However, the volume will change as the shape varies. Two NURBS (non-uniform rational b-spline) curves are fitted using these control points and the leading and trailing points. Figure 2 shows the control points and an approximation of the airfoil shape. The x coordinates of three top control points are fixed, which are 0.156869, 0.814025 and 0.952611, respectively. The x coordinates of three bottom control points are also fixed, which are 0.159457, 0.811269 and 0.951315, respectively. By varying the y coordinate of the control points, the airfoil shape could be changed.

Fig 2. Representation of Airfoil Shape
Using NURBS Curve

A two objective optimization was performed for the stated conditions: To maximize lift-to-drag (Cl/Cd) and to minimize entropy generation. The results are shown in Figure 3. As a note, because the optimization algorithm can only handle minimization, Cl/Cd was first calculated then its negative value is used as the objective function value. By doing this, minimizing negative Cl/Cd will be equivalent to maximizing Cl/Cd. The other objective is to minimize entropy generation, which is equivalent to minimizing drag as we stated previously. A genetic optimization algorithm [11] was modified and used in the study.

In Figure 3, each point represents an airfoil shape that is a feasible optimal solution. As maximizing Cl/Cd and minimizing entropy generation are different objectives, we see in the pareto range that entropy generation increases with Cl/Cd. This does not mean Cl/Cd always increases with the entropy generation. Each airfoil shown in Figure 3 is a compromise between Cl/Cd and entropy generation. Depending upon the preference, a designer could choose any of the airfoils.

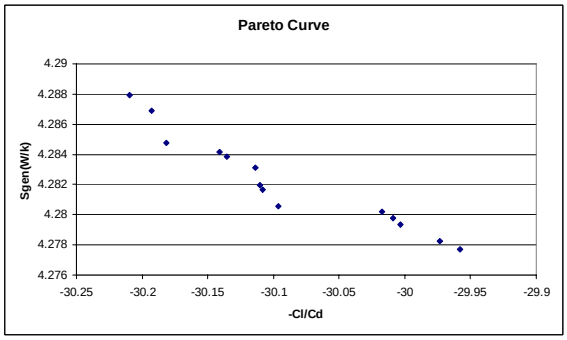

Fig 3. Pareto Curve of the Airfoil Shapes Optimization

3.2 3-D Wing CFD Results Comparisons

Three CFD finite wing models were constructed; two were geometrically twisted and the third was left untwisted. The two geometrically twisted wings were constructed to give elliptic and parabolic lift distributions. The untwisted wing was placed at an angle of attack to give the same lift as the other two wings. Lifting line theory was used to determine the geometric twist of the two twisted wings and was also used to determine the angle of attack the untwisted wing should be placed.

The wings were composed of NACA 0012 airfoil sections with a constant chord length. All three wings had a chord of 1 m and a span of 6 m, although a plane of symmetry was used at midspan so that only 3 m of the span had to be modeled. The flow conditions were Mach 0.2, Re_c=4,660,000 and at a temperature of 300 K and a pressure of 1 atm abs. The turbulence model used was the realizable k-ε model.

Before comparing the drag results of each wing it is important to note the respective resulting lift coefficients of each wing. All

three wings were designed, using lifting line theory, to have the same lift coefficient of 0.43. Two methods of determining lift from the CFD results were used. The first is the traditional surface integration technique where pressure and shear stress distributions are integrated and a resulting lift found. The second method is a wake integration technique described by Giles et al. [5][6]. The results of these lift calculations are shown in Table 3. In Table 3 it is seen that the parabolic wing deviates the most away from the theoretical lift coefficient using both methods of determining lift. The elliptic and untwisted wings agree more favorably with the theoretical lift coefficient as compared with the parabolic wing. These lift coefficients would of course be of importance when comparing relative Cl/Cd values between wings, however this comparison is not made here and the lift coefficients are provided only to make the reader aware.

Equation 9 allows the drag force of a wing to be computed by performing a volume integration within the CFD domain and a surface integral over the outlet of the CFD domain. The objective is, as mentioned above, to relate exergy destruction, or equivalently entropy generation, to drag. To do this the total entropy generation due to the presence of the wing must be determined if accurate drag values are to be obtained. Physically the volume integral in Equation 9 allows the entropy generation seen within the CFD domain to be determined. The surface integral acts to determine the entropy generation due to the wing that is not captured by the CFD domain. This is due to the fact that, in many cases, viscosity has yet to damp out all of the velocity perturbations on the exit plane of the CFD domain caused by the presence of the wing. Therefore the kinetic energy put into the air by the wing, for example in the wing tip vortex, must be determined realizing viscosity will eventually damp out these perturbations resulting in entropy generation. The idea here is that as the CFD domain extends further downstream of the wing the volume integral capturing entropy generation would increase and the surface integral, which captures the extra exergy destruction not seen in the CFD domain, would decrease. Therefore when the two components in Equation 9 are added together a constant drag force should be determined regardless how far the exit of the numerical model is aft of the wing. The limiting case would be when the numerical model captures the entire presence of the wing, in terms of entropy generation, and therefore the surface integral would be zero. As discussed earlier this is not likely since the computational requirements would be prohibitive for a numerical model this large.

To test this hypothesis the numerical model was separated into eight volumes. Each volume extends from the entrance of the numerical domain to a set distance aft of the wing. The volumes extend from one chord length behind the wing through consecutive integer chord lengths to eight chords behind the wing. For example, the first volume was composed of the entire numerical model from the front of the domain but only extended to one chord length behind the wing. In this case the surface integral was performed on a plane, perpendicular to the freestream velocity vector, one chord length behind the wing. The second volume is the same as the first but extended two chord lengths behind the wing and so on.

Figure 4 shows the increasing trend of entropy generation within the numerical model as the volume extends further downstream of the wing. This data agree with the expected increasing trend. The plot also shows the elliptic wing generating less entropy than the other two within the CFD domain modeled. Lifting line theory predicts the elliptic wing to have the minimum induced drag. Therefore the trend seen in the plot could be a result of the elliptic wing simply having less induced drag than the other two wings modeled.

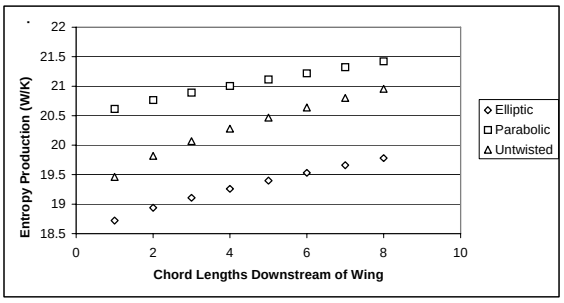

Fig 4. Entropy Production Within Numerical Volumes Extending the Indicated Length Downstream of the Wing

Figure 5 shows the total drag values calculated with Equation 9 on the numerical volume as it extends further downstream. The expected result is a constant drag value regardless of how far the numerical domain extends downstream. There is a slight overall decreasing trend as the numerical volume extends downstream. However the largest change in values is with the untwisted wing and that change is 8.4%. The largest change in the elliptic and parabolic wings is 4.6% and 2.5% respectively.

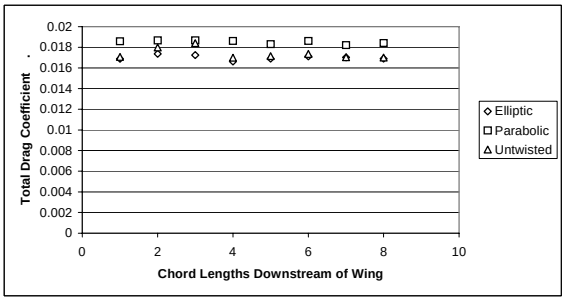

Fig. 5 Total Drag Coefficient Determined as the Numerical Volume Extends Further Downstream of Wing

The slight decreasing trend seen in Figure 5 may be due to artificial, or numerical, viscosity that is not accounted for in Equation 9. Artificial viscosity is a result of truncation error that arises from representing the fluid flow equations in discrete form. Since Equation 9 determines drag from velocity gradients and perturbation velocities it can be expected that any viscosity that is not accounted for in Equation 9 will contaminate the results. Therefore it can be expected that as more of the numerical volume is used in Equation 9 more error from numerical effects will occur. A solution to this problem would be to take the drag results given in the near field of the wing at say one or two chord lengths downstream of the wing. Another solution is to increase the grid density in the wake region. However more cells will require longer solution times and increased memory requirements. Second order solution schemes help to reduce artificial viscosity and were used in this study.

In the absence of experimental data a "semi-empirical" drag value was used to compare with drag values obtained from Equation 9. This semi-empirical value is so called because it is a combination of experimental 2-D wind tunnel results and Prandtl's lifting line induced drag estimate. Since induced drag is what separates drag on a two-dimensional airfoil from drag on a finite wing it is suggested to add the experimental two-dimensional drag coefficient to the theoretical induced drag coefficient predicted by lifting line theory for each wing to obtain a three-dimensional "semi-empirical" drag coefficient. The two-dimensional drag data is given as drag coefficients for various angles of attack [10]. The drag coefficient given for this airfoil at approximately the same Reynolds number and geometric angle of attack of the untwisted wing used in this study is 0.00785. The two-dimensional airfoil drag data was also used to obtain a two-dimensional drag coefficient for the elliptic and parabolic wings. This was accomplished by using an area-weighted average for the geometric angle distribution on each wing. The two-dimensional drag coefficient found using this method for the elliptic and parabolic wings is 0.0078 and 0.00792 respectively.

Table 4 shows the drag coefficients obtained from wing surface integration and the average value of eight numerical volumes from Equation 9 along with this semi-empirical drag value. The wing surface integration here refers to the method of integrating the surface pressure and shear stress distribution around

the wing to obtain a resultant drag value. The drag coefficient obtained by Equation 9 at one and two chord lengths downstream of the wing are also included.

Table 4 shows some expected trends. Drag calculated from wing surface integration was higher than both the semi-empirical value and the drag determined using Equation 9 for all three wings. As mentioned earlier this is most likely due to the boundary layer, which is assumed to be completely turbulent, and when combined with flat elements representing curved surfaces, may over predict drag due to the increased shear stress compared with laminar boundary layers. The average drag value obtained with the far-field method from one chord to eight chord lengths downstream of the wing agreed with the semi-empirical drag result to within 3.4%, 2.6%, and 4.4% for the elliptic, parabolic, and untwisted wing respectively. The best agreement with the semi-empirical value was obtained at two chord lengths behind the wing. The drag value determined using Equation 9 at two chord lengths behind each wing was within 1.1%, 1.6%, and 1.1% to the semi-empirical value for the elliptic, parabolic, and untwisted wing respectively. The agreement to the semi-empirical value was less desirable when Equation 9 was performed at one chord length behind each wing, however the largest difference was with the untwisted wing at 6%. The drag value obtained through wing surface integration was off from the semi-empirical value by 12.5%, 13.2%, and 8.8% for the elliptic, parabolic, and untwisted wing respectively.

The fact that Equation 9 predicts the closest agreement with the semi-empirical value when performed on a volume extending two chords behind the wing may be due to a number of factors. First it is fairly close to the wing resulting in a relatively smaller volume in which to integrate. This helps to reduce the effect of artificial viscosity simply because less of the numerical domain is included in the volume and surface integrations. However, this doesn't explain the difference between the one and two chord cases. One possible source of error in the one chord volume may be due to the relatively large gradients on the one chord plane as compared to the two chord plane thus potentially stressing the surface integration of Equation 9. No near field nor far field corrections are included in the results shown, however future research hopes to address this issue in an effort to achieve consistent drag values independent of the downstream plane location. In Destarac[3] and Bourdin's[2] study, they proposed a method to incorporate near-field and far-field corrections to the "apparent" reducing induced drag as the Treffiz plance moves away from the wing. Hunt et al. [6] have experienced the downstream plane dependency with their wake integration methods and have introduced cutoff parameters which attempts to determine the size of the wake plane needed while eliminating far field errors that may affect the results. They note however that artificial viscosity still has the effect of reducing predicted vortex drag values as the wake integration plane is moved further downstream.

4 Conclusion

An exergy-based method was introduced for use in an airfoil shape optimization scheme. Entropy generation minimization is coupled with a RANS-based numerical flow solver, a shape shifting algorithm and an optimizer to create a new design methodology. A two-objective optimization is performed to maximize lift/drag ratio and minimize entropy generated on simple airfoils under turbulent flow conditions. The resulting two objective pareto curve is a trade-off in shapes between larger lift/drag ratio and less exergy destruction.

A 3-D study was performed to extend the exergy-based methodology for linking drag to exergy destruction. A methodology for estimating drag with a RANS-based numerical flow solver in low speed flows was introduced. The methodology was applied to three test cases with the resulting drag value compared to

a semi-empirical drag value. The results, especially when taken from a CFD domain extending 2 chord lengths aft of the wing, agree well with the semi-empirical value for each wing. The results from the exergy-based method were in much better agreement with the semi-empirical value than the surface integration method of obtaining drag values.

5 References

[1] Bejan A. *Entropy Generation Minimization: The Method of Thermodynamic Optimization of Finite-Size Systems and Finite-Time Processes*. CRC Press, New York, 1996.

[2] Bourdin, P. Numerical predictions of wing-tip effects on lift-induced drag, ICAS 23rd Congress, Toronta, Canada, Vol. 2002, no. 168, 2002

[3] Destarac, D. Far-field / Near field Drag Balance and Applications of Drag Extraction in CFD. VKI Lecture Series 2003, CFD-based Aircraft Drag Prediction and Reduction, National Institute of Aerospace, Hampton (VA), 2003.

[4] Drost, MK and White, MD. Numerical Prediction of Local Entropy Generation in an Impinging Jet, *Journal of Heat Transfer*, vol. 113, pp 823-829, 1991.

[5] Giles, M and Cummings, R. Wake Integration for Three-Dimensional Flowfield Computations: Theoretical Development, *Journal of Aircraft*, 36, No. 2, pp 357-365, 1999.

[6] Hunt, H.L., Giles, M., and Cummings, R., Wake Integration for Three-Dimensional Flowfield Computations: Applications, *Journal of Aircraft*, **36**, No. 2, pp 366-373, 1999.

[7] Li, H and Figliola, RS. Exergy Based Design Methodology for Airfoil Shape Optimization, *10th AIAA/ISSMO Multidisciplinary Analysis and Optimization Conference*, Albany, New York. AIAA-2004-4632, 2004.

[8] Li, W and Krist, S. Transonic Airfoil Shape Optimization in Preliminary Design Environment, *10th AIAA/ISSMO Multidisciplinary Analysis and Optimization Conference*, Albany, New York. 2004.

[9] Shuja, SZ, Yilbas, BS and Budair, MO. Local Entropy Generation in an Impinging Jet: Minimum Entropy Concept Evaluating Various Turbulence Models, *Computer. Methods in Applied Mechanicss and Engineering*, vol. 190, pp 3623-3644, 2001.

[10] Sheldahl, RE and Klimas, PC. Aerodynamic Characteristics of Seven Airfoil Sections Through 180 Degrees Angle of Attack for Use in Aerodynamic Analysis of Vertical Axis Wind Turbines, Sandia National Laboratories, Albuquerque, New Mexico, SAND80-2114, March 1981.

[11] Srinivas, N and Deb, K. Multiobjective function optimization using nondominated sorting genetic algorithms, *Evolutionary Computation*, vol. 2, issue 3, pp 221-248, 1995.

Index	Model	Cd	Sgen	Cd deviation(%)	Sgen deviation(%)
0	Abid	0.008483	4.95319	26.61	8.24
1	Lam-Bremhorst	0.008368	4.94958	24.90	8.16
2	Launder-Sharma	0.011375	6.61105	69.77	44.46
3	Yang-Shih	0.007832	4.59388	16.90	0.38
4	Abe-Kondoh-Nagano	0.007317	4.31652	9.21	-5.68
5	Chang-Hsieh-Chen	0.007844	4.61249	17.07	0.79

Table 2 Drag comparison for NACA0012 airfoils with 6 Low-Re models

	Elliptic	Parabolic	Untwisted
Theory (Lifting Line)	0.43	0.43	0.43
Surface Integration	0.424	0.406	0.42
Average Wake Integral	0.437	0.408	0.432

Table 3 Lift Coefficients Determined by Indicated Method

	Elliptic	Parabolic	Untwisted
Semi-Empirical	0.0176	0.0190	0.0182
Surface Integration	0.0198	0.0215	0.0198
Equation 4.19 Average	0.0170	0.0185	0.0174
Equation 4.19 @ 1 Chord	0.0169	0.0186	0.0171
Equation 4.19 @ 2 Chord	0.0174	0.0187	0.0180

Table 4 Total Drag Coefficients Determined by Indicated Method